Integrated Motion Measurement for Flexible Structures

T. Örtel, J.F. Wagner

Integrated navigation, as an example of integrated motion measurement systems, is typically based on inertial sensors (accelerometers, gyros) and GPS and is commonly used for vehicle guidance. Traditionally, the vehicle of integrated navigation systems is assumed to be a rigid body. However, extending these integrated systems to elastic structures is possible. The considered continuum, in particular a flexible beam, is an attempt to obtain motion measurements of an aerofoil of a flying aircraft with large structural dimensions. Integrated systems considered here in general are fusing different measuring methods by using their benefits and blinding out their disadvantages. For instance, gyros and accelerometers are used to obtain reliable signals with a good time resolution. On the other hand, aiding sensors like radar units and strain gauges are known to be long-term accurate. The kernel of the integrated systems presented in this article consists, however, of an continuous-discrete extended Kalman filter estimating the motion state of the structure. Besides the sensor signals to be amalgamated, the filter requires a kinematical model of the vehicle motion considered, which has to be developed individually. This kinematical model describes the standardised dynamics of the vehicle by means of specific forces, i.e. accelerations, and of rotational velocities. Thus, there are no dynamometers or mass and stiffness properties needed in this approach. Diverse kinematical models of the beam were developed and evaluated, using model reduction in regard of the natural modes. Based on simulation the paper shows this approach, appropriate sensor sets, and estimated motion results of a flexible beam.

1 Introduction

Integrated navigation devices for vehicle guidance are the most common example of an integrated motion measurement system combining the signals from an inertial measurement unit (three accelerometers, three gyros) and a GPS receiver with a single antenna. Traditionally, for these systems the vehicle is assumed to be a single rigid body with six motional degrees of freedom to be determined (Farrell and Barth (1999)). During periods of low vehicle dynamics the common integrated navigation systems show stability problems due to a loss of observability (see section 2.3). Nevertheless, the stability of the system can be guaranteed by distributing additional sensors over the vehicle structure. However, in this case the rigid body assumption has to be expanded to take the distributed sensors and the flexibility of the structure into account. Integrated systems using distributed sensors and considering consequently the flexibility of the structure are not state of the art (Quinn et al. (2005)) and will be investigated in this article.

Integrated systems in general are fusing different measuring signals by combining their advantages and blinding out their disadvantages. For instance, gyros and accelerometers are used to obtain reliable signals with a good time resolution. On the other hand, aiding sensors like radar units and strain gauges are known to be long-term accurate. Furthermore, the kernel of the integrated systems consists of an extended Kalman filter that estimates the motion state of the structure (see section 2.2). Besides the sensor signals, the basis for the filter is an additional kinematical model of the structure which has to be developed individually. The example of the motion of an elastic beam being considered here is meant to be an approach to obtain motion measurements of a wing of a large airplane during flight. This investigation aims not only on an extensive motion control but also on system identification and structural monitoring.

In the following chapter 2 the basics of integrated measurement systems are explained. Chapter 3 generalises the theory of integrated navigation systems for flexible structures. It includes an example of a kinematical model of a flexible beam. Chapter 4 will focus on the model reduction of the considered beam and will explain in more detail the concept of the modal approach. The quality of the filter estimation results depends decisevely on the position of the sensors. Therefore, sensor positioning was adapted using the information of the mode shapes which is also explained in chapter 4. Chapter 5 shows the estimated motion results of the beam, and an outlook of the future topics to be investigated is given in chapter 6.

2 Integrated Navigation and Motion Measurement Systems

Utilising integrated navigation systems was generally thought to be expensive and difficult to handle due to sophisticated gyro technology and numerically error-proneness. Nowadays, the meaning of classical inertial platforms is decreasing in favour of micromechanical and optical sensors. The combination of different sensors is handled with mathematical algorithms, usually an extended Kalman filter, implemented on efficient micro-processors. The signal fusion helps to reduce numerical error-proneness of the system, which makes the use of worse but cost-saving inertial sensors possible.

Integrated navigation systems are no longer exclusively used for military and aviation purposes, as can be seen on the common commercial car navigation systems. The most typical layout of an integrated navigation system is a combination of an Inertial Measurement Unit (IMU), that includes three accelerometers and gyros respectively, and a single GPS receiver. The vehicle is assumed to be a rigid body with six mechanical degrees of freedom to be determined. These typical systems show stability problems during phases of weak vehicle dynamics (i.e. almost constant translative velocity or low angular rate), which is due to the loss of system observability. Multiple spaciously distributed GPS antennas enhance the system accuracy. Additionally, filter stability is increased effectively (Wagner (2003)). However, integrated navigation systems in large vehicles with structural deformations infringe the assumption of a rigid body. Therefore, methods will be presented to take the flexure effects into account.

Section 2.1 will concentrate on the observer principle which is the basis for integrated measurement systems. A typical realisation of the observer principle is the extended Kalman filter. The theory and algorithm of the Kalman filter will be presented in section 2.2. Afterwards, the condition of observability of the state vector is shown in the following subsection. Chapter 2 is finished giving an example of a rigid mulitbody system.

2.1 Principle of Integrated Motion Measurement

The idea of integrated navigation systems consists of combining complementary motion measuring principles and utilising their specific advantages: Inertial sensors like classical or modern micro-electromechanical gyros and accelerometers are used to obtain reliable signals allowing a high resolution with time. On the other hand, less dependable sensors (often with relevant signal delays) like GPS receivers and radar units are used due to their good long-term accuracy. The kernel of integrated navigation systems is an observer (typically realised by an extended Kalman filter (Gelb (1989), Wagner (2003))) blending the sensor signals and estimating the relevant vehicle motion (Farrell and Barth (1999)). Therefore, integrated navigation systems are strictly speaking integrated motion measurement systems.

Besides the sensor combination employed, the theoretical basis for the filter requires a kinematical model of the vehicle motion considered, which has to be set up individually (nevertheless, well established models exist (Wagner and Wieneke (2003))). This model describes the standardised dynamics of the vehicle, mostly by means of specific forces, i.e. accelerations, and of angular rates. Hence, there are no dynamometers or mass and stiffness properties needed in this approach.

There are different system integration variants of such navigation systems (Wagner and Wieneke (2003)). However, they all have the observer principle in common with the signal flow depicted in Figure 1: Reliable sensors like accelerometers and gyros provide the input signal vector $\mathbf{u}$ generating the vehicle motion considered (state vector $\mathbf{x}$). Based on $\mathbf{x}$ and $\mathbf{u}$, so-called aiding sensors (being mostly attached to the vehicle) like a GPS receiver or a radar altimeter provide the measurement vector $\mathbf{y}$. Furthermore, there is a parallelism between the performance of the real moving structure and its aiding equipment on one side and a motion and aiding simulation on the other side which leads to estimates $\hat{\mathbf{x}}$ and $\hat{\mathbf{y}}$ of $\mathbf{x}$ and $\mathbf{y}$.
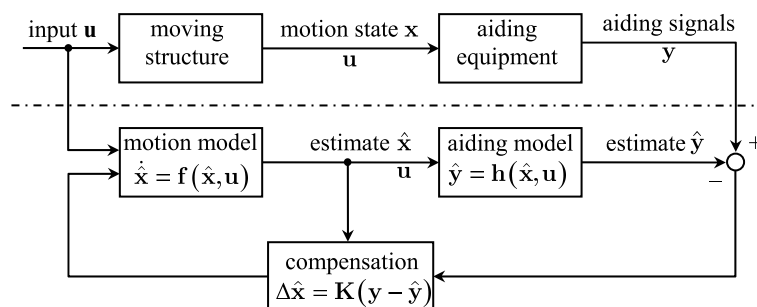
Figure 1: Observer Principle.

Due to sensor, modelling and initialisation errors, the estimates show inaccuracies, which increase usually with time t and which require therefore a correction: The feedback of the difference between $\mathbf{y}$ and $\hat{\mathbf{y}}$ serves as input of a compensation device adjusting the estimate $\hat{\mathbf{x}}$ by $\mathbf{K}(\mathbf{y} - \hat{\mathbf{y}})$. The correction matrix $\mathbf{K}(t)$ is typically part of the algorithm of an extended Kalman filter, however sometimes alternatives like particle filters are used as well (Yi and Grejner-Brzezinska (2006)).

2.2 Extended Kalman Filter

As already mentioned above, the observer principle is typically realised by an extended Kalman filter. The latter one uses noisy signals as input $\mathbf{u}$ and calculates a smooth estimate $\hat{\mathbf{x}}$ of the state vector $\mathbf{x}$. The basis for the extended Kalman filter are two models describing the motion considered. The first one, the motion model, is a set of ordinary nonlinear differential equations (being solved numerically), the second one, the aiding model, is a set of algebraic equations.

$$\dot{\mathbf{x}}(t) = \mathbf{f}\left(\mathbf{x}(t), \mathbf{u}(t)\right) + \mathbf{G}\left(\mathbf{x}(t), \mathbf{u}(t)\right) \cdot \mathbf{w}(t) \,, \qquad \dot{\hat{\mathbf{x}}}(t) = \mathbf{f}\left(\hat{\mathbf{x}}(t), \mathbf{u}(t)\right) \,, \tag{1}$$

$$\mathbf{y}(t) = \mathbf{h}\left(\mathbf{x}(t)\right) + \mathbf{v}(t) \,, \qquad\qquad\qquad \hat{\mathbf{y}}(t) = \mathbf{h}\left(\hat{\mathbf{x}}(t), \mathbf{u}(t)\right) \,. \tag{2}$$

Vector $\mathbf{v}$ can be interpreted as the measurement noise of the aiding. The term $\mathbf{G} \cdot \mathbf{w}$ is the compensation of the noise of the input $\mathbf{u}$. It has to be assumed that the following stochastic relations of $\mathbf{w}$, $\mathbf{v}$ and $\mathbf{x}(0)$ apply, with t and τ being different points in time.

$$\mathrm{E}\left[\mathbf{w}(t)\right] \equiv \mathbf{0} \,, \quad \mathrm{E}\left[\mathbf{v}(t)\right] \equiv \mathbf{0} \,, \tag{3}$$

$$\mathrm{E}\left[\mathbf{x}(0)\right] = \mathbf{x}_0 \,, \tag{4}$$

$$\mathrm{E}\left[\mathbf{w}(t) \cdot \mathbf{v}^T(\tau)\right] \equiv \mathbf{0} \,, \quad \mathrm{E}\left[\mathbf{w}(t) \cdot \mathbf{x}^T(0)\right] \equiv \mathbf{0} \,, \quad \mathrm{E}\left[\mathbf{v}(t) \cdot \mathbf{x}^T(0)\right] \equiv \mathbf{0} \,. \tag{5}$$

Furthermore, the theory of the Kalman Filter requires, that $\mathbf{v}$ and $\mathbf{w}$ are made up of white noise, which causes the appearance of the Dirac δ-function.

$$\mathrm{E}\left[\mathbf{w}(t) \cdot \mathbf{w}^T(\tau)\right] = \mathbf{Q}(t)\,\delta(t - \tau) \,, \tag{6}$$

$$\mathrm{E}\left[\mathbf{v}(t) \cdot \mathbf{v}^T(\tau)\right] = \mathbf{R}(t)\,\delta(t - \tau) \,, \tag{7}$$

$$\mathrm{E}\left[\left(\mathbf{x}(t) - \hat{\mathbf{x}}(t)\right)\left(\mathbf{x}(t) - \hat{\mathbf{x}}(t)\right)^T\right] = \mathbf{P}(t) \,, \tag{8}$$

$$\mathrm{E}\left[\left(\mathbf{x}(0) - \mathbf{x}_0\right)\left(\mathbf{x}(0) - \mathbf{x}_0\right)^T\right] = \mathbf{P}_0 \,. \tag{9}$$

$\mathbf{Q}$, $\mathbf{R}$ and $\mathbf{P}$ shall be symmetric and positive definite matrices. The matrix $\mathbf{Q}$ is diagonal. Since the measurement devices are sample units, the following equations are also given in intervals. The depiction t_{k-1} and t_k describes the time between two consecutive measuring points. The notation $t|t_{k-1}$ means, that the considered time t lies in the interval t_{k-1} and t_k. The filter equations are composed of three parts. The first one initialises the algorithm.

$$\hat{\mathbf{x}}(0|0) = \mathbf{x}_0 \,, \tag{10}$$

$$\mathbf{P}(0|0) = \mathbf{P}_0 \,. \tag{11}$$

The second part of the filter equations estimates $\hat{\mathbf{x}}$ and $\mathbf{P}$ in an interval t_{k-1} and t_k without using an update of the aiding system. The integration of the following equations is realised for example with a Runge-Kutta method of the fourth order. In the following, matrix $\mathbf{F}$ and $\mathbf{H}$ represent the Jacobians of $\mathbf{f}$ and $\mathbf{h}$.

$$\dot{\hat{\mathbf{x}}}(t|t_{k-1}) = \mathbf{f}\left(\hat{\mathbf{x}}(t|t_{k-1}), \mathbf{u}(t|t_{k-1})\right) \,, \tag{12}$$

$$\dot{\mathbf{P}}(t|t_{k-1}) = \mathbf{F}\left(\hat{\mathbf{x}}(t|t_{k-1}), \mathbf{u}(t|t_{k-1})\right) \cdot \mathbf{P}(t|t_{k-1}) \tag{13}$$
$$+ \ \mathbf{P}(t|t_{k-1}) \cdot \mathbf{F}^T\left(\hat{\mathbf{x}}(t|t_{k-1}), \mathbf{u}(t|t_{k-1})\right)$$
$$+ \ \mathbf{G}\left(\hat{\mathbf{x}}(t|t_{k-1}), \mathbf{u}(t|t_{k-1})\right) \cdot \mathbf{Q}(t|t_{k-1}) \cdot \mathbf{G}^T\left(\hat{\mathbf{x}}(t|t_{k-1}), \mathbf{u}(t|t_{k-1})\right) \,.$$

The third part of the filter equations is due to the update of the aiding equipment. Furthermore, the aiding signals will be processed sequentially, that helps to avoid a time-consuming matrix inversion. Shall $n_{\mathbf{y}}$ aiding signals be available at time t_k, thus there are $\iota = 1, \ldots, n_{\mathbf{y}}$ single steps to be carried out. $\mathbf{K}(t_{k,\iota})$ is the filter matrix for each step ι. Furthermore $\mathbf{H}_{\iota}$ shall be the ιth row of $\mathbf{H}$ and R_{ι} shall be the ιth diagonal element of $\mathbf{R}$. With $t_k|t_{k,0} = t_k|t_{k-1}$ and $\mathbf{I}$ symbolising the unit matrix, the estimate $\hat{\mathbf{x}}$ after including an aiding signal can be derived

as the following.

$$\hat{\mathbf{x}}(t_k|t_{k,\iota}) = \hat{\mathbf{x}}(t_k|t_{k,\iota-1}) + \mathbf{K}(t_{k,\iota}) \cdot (y_\iota(t_k) - h_\iota \left(\hat{\mathbf{x}} \left(t_k|t_{k,\iota-1} \right) \right)) \,, \tag{14}$$

$$\mathbf{K}(t_{k,\iota}) = \frac{\mathbf{P}(t_k|t_{k,\iota-1}) \cdot \mathbf{H}_\iota^T(\hat{\mathbf{x}}(t_k|t_{k,\iota-1}))}{\mathbf{H}_\iota(\hat{\mathbf{x}}(t_k|t_{k,\iota-1})) \cdot \mathbf{P}(t_k|t_{k,\iota-1}) \cdot \mathbf{H}_\iota^T(\hat{\mathbf{x}}(t_k|t_{k,\iota-1})) + R_\iota(t_k)} \,, \tag{15}$$

$$\mathbf{P}(t_k|t_{k,\iota}) = \mathbf{K}(t_{k,\iota}) \cdot R_\iota(t_k) \cdot \mathbf{K}^T(t_{k,\iota}) \tag{16}$$
$$+ (\mathbf{I} - \mathbf{K}(t_{k,\iota}) \cdot \mathbf{H}_\iota(\hat{\mathbf{x}}(t_k|t_{k,\iota-1}))) \cdot \mathbf{P}(t_k|t_{k,\iota-1}) \cdot (\mathbf{I} - \mathbf{K}(t_{k,\iota}) \cdot \mathbf{H}_\iota(\hat{\mathbf{x}}(t_k|t_{k,\iota-1})))^T \,.$$

After the last correction step $\iota = n_\mathbf{y}$ of the third part $t_k|t_{k,n_\mathbf{y}} = t_k|t_k$ has to be applied to start a new interval. For a more sophisticated insight in the theory of the presented continuous-discrete extended Kalman filter see Gelb (1989).

2.3 Observability

Independently from the observer type, the system stability requires that the state vector $\mathbf{x}$ is completely observable. This means that the correction $\mathbf{K}(\mathbf{y} - \hat{\mathbf{y}})$ acts appropriately on all components of $\hat{\mathbf{x}}$. Reflecting the type and geometrical array of the sensors used, the content of $\mathbf{f}$ and $\mathbf{h}$ determines this property. The observability is ensured if the matrix

$$\mathbf{\Xi} = \left[\begin{array}{cccc} \mathbf{H}^T & \mathbf{F}^T \cdot \mathbf{H}^T & \dots & \left(\mathbf{F}^T \right)^{n_\mathbf{x}-1} \cdot \mathbf{H}^T \end{array} \right] \tag{17}$$

employing the Jacobians $\mathbf{F}(\mathbf{x}(t), \mathbf{u}(t))$ and $\mathbf{H}(\mathbf{x}(t))$ of $\mathbf{f}$ and $\mathbf{h}$ has full rank $n_\mathbf{x}$ (Gelb (1989)), with $n_\mathbf{x}$ being the number of state variables in $\mathbf{x}$. As $\mathbf{F}$ and $\mathbf{H}$ vary with time, it is possible that phases of complete observability alternate with phases of reduced observability. During reduced observability periods the error of estimates $\hat{\mathbf{x}} - \mathbf{x}$ and the elements of $\mathbf{P}$ increase causing possibly an unstable system. This applies especially for the classical combination of inertial sensors with a single antenna GPS receiver during periods of steady vehicle motion.

2.4 Example of a Rigid Multibody System

To illustrate the statements given above Figure 2 shows an example of a multibody system. Two stiff rods (length l_1, l_2) are pivoted to each other. The end A of the upper rod is freely swivelling and slides additionally on a rail. Furthermore, point A is connected to a wall with a spring. The transverse distance q_1 and the angular positions q_2, q_3 are the generalised coordinates of the structure. The system is equipped with two accelerometers attached at the lower joint (u_1, u_2) and two gyros (u_3, u_4) at each rod. The aiding equipment consists of three radar units measuring the distances ρ_1, ρ_2, ρ_3. The following relations below describe the kinematical behaviour of the structure. The state vector $\mathbf{x}$ is the following:

$$\mathbf{x} = \left[\begin{array}{cccc} q_1 & q_2 & q_3 & \dot{q}_1 \end{array} \right]^T = \left[\begin{array}{cccc} x_1 & x_2 & x_3 & x_4 \end{array} \right]^T \,. \tag{18}$$

The directly measurable quantities $\dot{q}_2$ and $\dot{q}_3$ are omitted in $\mathbf{x}$, they are found instead in the input vector $\mathbf{u}$.:

$$\mathbf{u} = \left[\begin{array}{ccccc} u_1 & u_2 & u_3 & u_4 & \dot{u}_3 \end{array} \right]^T \,. \tag{19}$$

The additional time derivative of u_3 is needed, which is due to fictitious forces at the accelerometer attachment point. This is new compared to classical inertial navigation systems. The additional signal u_3 can be generated by numerically differentiating the angular velocity signals or by new sensors (STM (2004)). The function $\mathbf{f}$ reads:

$$\mathbf{f}(\mathbf{x}, \mathbf{u}) = \left[\begin{array}{c} x_4 \\ u_3 \\ u_4 \\ (u_1 - l_1 \dot{u}_3) \cos x_2 - (u_2 - l_1 u_3^2) \sin x_2 \end{array} \right] \,. \tag{20}$$

Regarding the fourth row of $\mathbf{f}$, the effect of angular acceleration and the centripetal acceleration can be seen. However, the displacing influence of gravity $\mathbf{g}$ cancels out.
The aiding vector $\mathbf{y}$ consists of three distance measurements:

$$\mathbf{y} = \left[\begin{array}{ccc} \rho_1 & \rho_2 & \rho_3 \end{array} \right]^T = \left[\begin{array}{ccc} y_1 & y_2 & y_3 \end{array} \right]^T \,. \tag{21}$$

The aiding model can be directly derived from the geometry of Figure 2.

$$\mathbf{h}(\mathbf{x}) = \left[\begin{array}{c} d - x_1 \\ d - x_1 - l_1 \sin x_2 \\ d - x_1 - l_1 \sin x_2 - l_2 \sin x_3 \end{array} \right] \tag{22}$$
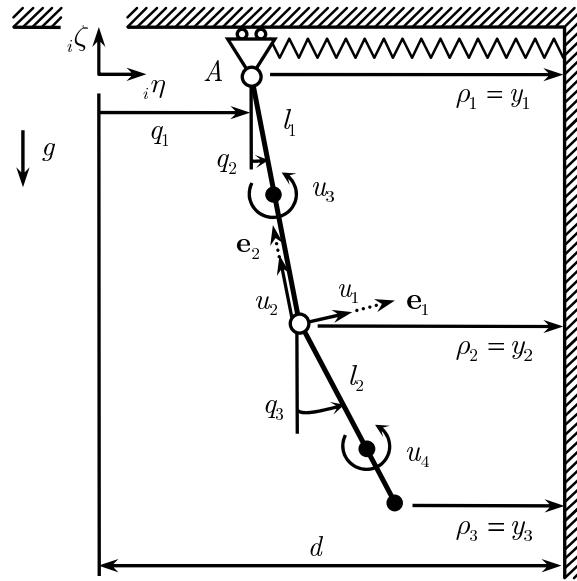
Figure 2: Double pendulum.

Prepared by simulated measurements the arrangement of Figure 2 was experimentally realised in order to test its functionality and performance. Exemplarily, Figure 3 compares the aiding signal ρ_1 and the estimated transverse distance $\hat{q}_1$ for the pendulum being at rest. All of the sensors used were products designed for mass markets with an accuracy of 0.05 m/s^2 (accelerometers), 0.2 $°$/s (gyros), 0.02 m (radar noise), and 2 m (radar jamming). Nevertheless, the remaining noise of the estimate is remarkably low. More information about the modelling prodedure and detailed results can be found in Wagner (2004).

3 Flexible Structures

Using integrated measurement systems for structures with large dimensions and distributed sensors, the flexure cannot be neglected anymore. The varying shape of the structure has to be taken into account and must be included in the kinematical model. The following sections will present a method that describes the flexible character of a structure with means of deformation variables. An example of a kinematical model of a beam structure is shown idealising a wing of an aircraft during flight. But first, the procedure for creating kinematical models using accelerometers, gyros, and aiding devices as peripheral sensors will be explained in detail. Section 3.1 will focus on accelerometers as peripheral sensors, the following subsection on gyros as peripheral sensors. Examples of integrated motion measurement systems for a flexible beam are presented in sections 3.4 to 3.6.

Figure 4 represents the exemplary initial point of the corresponding theory for flexible structures. It shows an aircraft fuselage with an exaggeratedly distorted wing half attached, the original wing shape being indicated by the dashed line. A body-fixed coordinate system b with origin B serves for describing the time-variant structural geometry. An IMU is located at B measuring the inertial (derivation system index i) acceleration ${}^i\ddot{\mathbf{r}}_B$ and the
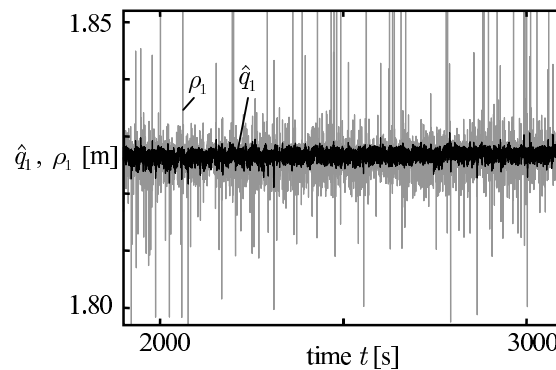
Figure 3: Comparison of the estimate $\hat{q}_1$ and of ρ_1 for the pendulum of Figure 2 being at rest.

98
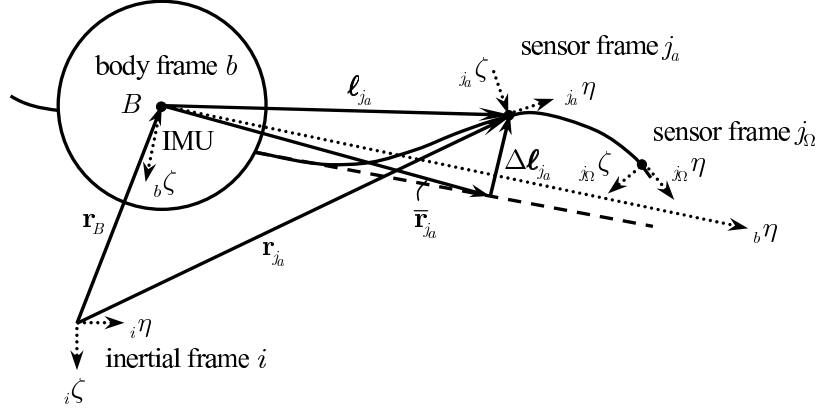
Figure 4: Aircraft fuselage cross section with distorted wing half and peripheral sensors a_j and Ω_j.

inertial angular rate $\boldsymbol{\omega}_{bi}$. Furthermore, additional accelerometers $j_a = 1, \ldots, \nu_a$ and further gyros $j_\Omega = 1, \ldots, \nu_\Omega$ are placed on the wing measuring the acceleration a_j and the angular rate Ω_j in the sensor frames.

3.1 Accelerometers as Peripheral Sensors

Having Figure 4 in mind, the accelerometer attachment points are subject to the acceleration

$$ {}^i\ddot{\mathbf{r}}_{j_a} = {}^i\ddot{\mathbf{r}}_B + {}^b\ddot{\boldsymbol{\ell}}_{j_a} + 2(\boldsymbol{\omega}_{bi} \times {}^b\dot{\boldsymbol{\ell}}_{j_a}) + {}^i\dot{\boldsymbol{\omega}}_{bi} \times \boldsymbol{\ell}_{j_a} + \boldsymbol{\omega}_{bi} \times (\boldsymbol{\omega}_{bi} \times \boldsymbol{\ell}_{j_a}) \,. \tag{23} $$

In this equation, $\mathbf{r}_B$ is an inertial position vector, and $\boldsymbol{\ell}_{j_a}$ denotes the actual lever arm between the IMU and any peripheral sensor. Again, the superscript on the left side indicates the coordinate system, in which the differentiation takes place. The angular rate $\boldsymbol{\omega}_{bi}$ describes (as already indicated) the angular velocity between the body and the inertial frames b and i. As mentioned, the change of angular rate ${}^i\dot{\boldsymbol{\omega}}_{bi}$ can be achieved by differentiating the signal of the angular rate or by new sensors types that measure directly the angular rate.

Assuming furthermore small distortions of the structure (a presumption being largely adequate for flexible vehicles), the actual lever arm $\boldsymbol{\ell}_{j_a}$ and its body oriented time derivatives can be approximated by a finite series reflecting e.g. the main vibration modes:

$$ \boldsymbol{\ell}_{j_a}(t) = \bar{\mathbf{r}}_{j_a} + \Delta\boldsymbol{\ell}_{j_a}(t) \quad \approx \quad \bar{\mathbf{r}}_{j_a} + \sum_{\chi=1}^{\Gamma_a} b_\chi(t)\,\mathbf{s}_\chi(\bar{\mathbf{r}}_{j_a}) \,, \tag{24} $$

$$ {}^b\dot{\boldsymbol{\ell}}_{j_a}(t) = {}^b\Delta\dot{\boldsymbol{\ell}}_{j_a}(t) \quad \approx \quad \sum_{\chi=1}^{\Gamma_a} \dot{b}_\chi(t)\,\mathbf{s}_\chi(\bar{\mathbf{r}}_{j_a}) \,, \tag{25} $$

$$ {}^b\ddot{\boldsymbol{\ell}}_{j_a}(t) = {}^b\Delta\ddot{\boldsymbol{\ell}}_{j_a}(t) \quad \approx \quad \sum_{\chi=1}^{\Gamma_a} \ddot{b}_\chi(t)\,\mathbf{s}_\chi(\bar{\mathbf{r}}_{j_a}) \,. \tag{26} $$

All time dependent amplitudes $b_\chi(t)$ represent extra degrees of freedom, all $\mathbf{s}_\chi(\bar{\mathbf{r}}_{j_a})$ are the vectorial descriptions of Γ_a deformation modes selected for describing the structural distortions. Besides, every of these functions of the structural position $\bar{\mathbf{r}}_{j_a}$ is defined to have at least at one point the displacement value 1. Thus, the additional degree of freedom $b_\chi(t)$ is the resultant position shift of this point if only the respective mode of the unit deformation $\mathbf{s}_\chi$ is excited (Figure 5).

It has to be taken into account that accelerometer signals include the negative gravity $\mathbf{g}$. Therefore, the following compensation equations have to be considered. The subscript on the left indicates the coordinate systems in which the measurement takes place. The matrices ${}_{j_ae}\mathbf{T}$ and ${}_{be}\mathbf{T}$ describe the transformation between the earth fixed system e, here the inertial system i, and the sensor and body system respectively.

$$ {}_{j_a}\mathbf{a}_{j_a} \;=\; {}_{j_a}^{i}\ddot{\mathbf{r}}_{j_a} - {}_{j_ae}\mathbf{T}\,{}_e\mathbf{g} \,, \tag{27} $$

$$ {}_b\mathbf{a}_B \;=\; {}_b^{i}\ddot{\mathbf{r}}_B - {}_{be}\mathbf{T}\,{}_e\mathbf{g} \,. \tag{28} $$

99
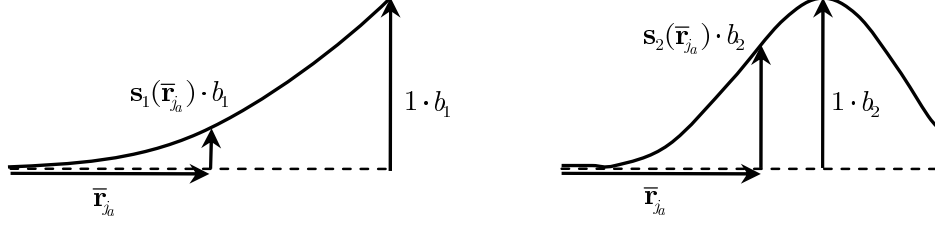
Figure 5: Concept of unit deformations and additional degrees of freedom.

Introducing equations (24) - (28) into (23) for all ν_a accelerometers and using the abbreviation for $\mathbf{s}_\chi(\bar{\mathbf{r}}_{j_a}) = \mathbf{s}_{\chi,j_a}$ yields the following:

$$
{}^i_{j_a}\ddot{\mathbf{r}}_{j_a} = {}_{j_a}\mathbf{a}_{j_a} + {}_{j_ae}\mathbf{T}\,_e\mathbf{g} \quad = \quad {}_{j_ab}\mathbf{T}\left\{{}_b\mathbf{a}_B + {}_{be}\mathbf{T}\,_e\mathbf{g} + \sum_{\chi=1}^{\Gamma_a}\ddot{b}_\chi(t)\,_b\mathbf{s}_{\chi,j_a}\right.
\tag{29}
$$

$$
+ 2\left({}_b\boldsymbol{\omega}_{bi} \times \sum_{\chi=1}^{\Gamma_a}\dot{b}_\chi(t)\,_b\mathbf{s}_{\chi,j_a}\right) + {}^i_b\dot{\boldsymbol{\omega}}_{bi} \times \left({}_b\bar{\mathbf{r}}_{j_a} + \sum_{\chi=1}^{\Gamma_a}b_\chi(t)\,_b\mathbf{s}_{\chi,j_a}\right)
$$

$$
\left. + {}_b\boldsymbol{\omega}_{bi} \times \left({}_b\boldsymbol{\omega}_{bi} \times \left({}_b\bar{\mathbf{r}}_{j_a} + \sum_{\chi=1}^{\Gamma_a}b_\chi(t)\,_b\mathbf{s}_{\chi,j_a}\right)\right)\right\}.
$$

After rearranging equation (29) can be written as a set of linear function with respect to $\ddot{b}_\chi$.

$$
{}_{j_a}\mathbf{a}_{j_a} - {}_{j_ab}\mathbf{T}\,_b\mathbf{a}_B - {}_{j_ab}\mathbf{T}\left({}^i_b\dot{\boldsymbol{\omega}}_{bi} \times {}_b\bar{\mathbf{r}}_{j_a} + {}_b\boldsymbol{\omega}_{bi} \times \left({}_b\boldsymbol{\omega}_{bi} \times {}_b\bar{\mathbf{r}}_{j_a}\right)\right) =
\tag{30}
$$

$$
{}_{j_ab}\mathbf{T} \cdot \sum_{\chi=1}^{\Gamma_a}\left\{\ddot{b}_\chi\,_b\mathbf{s}_{\chi,j_a} + 2\dot{b}_\chi\left({}_b\boldsymbol{\omega}_{bi} \times {}_b\mathbf{s}_{\chi,j_a}\right) + b_\chi({}^i_b\dot{\boldsymbol{\omega}}_{bi} \times {}_b\mathbf{s}_{\chi,j_a} + {}_b\boldsymbol{\omega}_{bi} \times \left({}_b\boldsymbol{\omega}_{bi} \times {}_b\mathbf{s}_{\chi,j_a}\right))\right\}
$$

If $\nu_a = \Gamma_a$ holds and the sensors are placed appropriately, solving this set of equations for each single $\ddot{b}_\chi$ is possible (if $\nu_a > \Gamma_a$ holds, the employment of a Least Squares procedure is viable, compare equation (44) below). Composing now the state vector $\mathbf{x}$ of all b_χ and their first time derivatives, the composition of $\mathbf{f}(\mathbf{x}, \mathbf{u})$ (see equation (1)) follows directly. However, a completion of $\mathbf{f}$ by the classical equations of an inertial navigation system is also necessary (Wagner (2003)). Then, the input vector $\mathbf{u}$ contains all signals of the IMU and of the peripheral accelerometers. Taking the component of the vector equation (30) describing the measurement direction of the accelerometer and solving for $\ddot{b}_\chi$ yields:

$$
\ddot{b}_\chi = \sum_{j_a=1}^{\nu_a} f^*_{j_a}\left({}_{j_a}\mathbf{a}_{j_a}, {}_b\mathbf{a}_B, {}_{j_ab}\mathbf{T}, {}_b\boldsymbol{\omega}_{bi}, {}_b\dot{\boldsymbol{\omega}}_{bi}, {}_b\bar{\mathbf{r}}_{j_a}, \dot{b}_{\bar\chi}, b_{\bar\chi}, {}_b\mathbf{s}_{\bar\chi,\bar{j}_a}\right) \quad \text{with} \left\{\begin{array}{l} \chi = 1, ..., \Gamma_a \\ \bar\chi = 1, ..., \Gamma_a \\ \bar{j}_a = 1, ..., \nu_a \end{array}\right. .
\tag{31}
$$

3.2 Gyros as Peripheral Sensors

Instead of accelerometers, the use of gyros as input sensors is also feasible. Figure 4 shows besides the accelerometer also a gyro j_Ω, that is subject to the angular velocity

$$
\boldsymbol{\omega}_{j_\Omega i} = \boldsymbol{\omega}_{bi} + \frac{1}{2}\frac{\mathrm{d}}{\mathrm{d}t}\left(\text{curl}\,\Delta\boldsymbol{\ell}_{j_\Omega}\right).
\tag{32}
$$

The lever arm $\Delta\boldsymbol{\ell}_{j_\Omega}(t)$ is again approximated by a series using different functions $\mathbf{s}_\chi$ with $\chi = \Gamma_a + 1, \ldots, \Gamma_a + \Gamma_\Omega$:

$$
\Delta\boldsymbol{\ell}_{j_\Omega}(t) = \sum_{\chi=1+\Gamma_a}^{\Gamma_a+\Gamma_\Omega} b_\chi(t)\,\mathbf{s}_\chi(\bar{\mathbf{r}}_{j_\Omega}).
\tag{33}
$$

Putting equation (32) and (33) together and writing the result with respect to the sensor system j_Ω, which is indicated again with the subscript on the left side, yields the following with $\mathbf{s}_\chi(\bar{\mathbf{r}}_{j_\Omega}) = \mathbf{s}_{\chi,j_\Omega}$.

$$
{}_{j_\Omega b}\mathbf{T} \cdot \sum_{\chi=1+\Gamma_a}^{\Gamma_a+\Gamma_\Omega}\dot{b}_\chi(t)\,\text{curl}\,_b\mathbf{s}_{\chi,j_\Omega} = 2\left({}_{j_\Omega}\boldsymbol{\omega}_{j_\Omega i} - {}_{j_\Omega b}\mathbf{T}\,_b\boldsymbol{\omega}_{bi}\right)
\tag{34}
$$

100

Equation (34) is now linear with respect to $\dot{b}_\chi(t)$. For $\nu_\Omega \geq \Gamma_\Omega$ and well positioned gyros, solving for $\dot{b}_\chi$ is possible taking the rotational component of equation (34).

$$\dot{b}_\chi = \sum_{j_\Omega=1}^{\nu_\Omega} f_{j_\Omega}^* \left({}_{j_\Omega b}\mathbf{T}, {}_{j_\Omega}\boldsymbol{\omega}_{j_\Omega i}, {}_{b}\boldsymbol{\omega}_{bi}, \operatorname{curl} {}_{b}\mathbf{s}_{\bar{\chi},\bar{j}_\Omega} \right) \quad \text{with} \quad \begin{cases} \chi = 1+\Gamma_a, ..., \Gamma_a + \Gamma_\Omega \\ \bar{\chi} = 1+\Gamma_a, ..., \Gamma_a + \Gamma_\Omega \\ \bar{j}_\Omega = 1, ..., \nu_\Omega \end{cases} \tag{35}$$

The state vector $\mathbf{x}$ of a model using peripheral gyros contains solely the additional variables b_χ, however, $\mathbf{x}$ of kinematical models utilising peripheral accelerometers contains b_χ and $\dot{b}_\chi$. Furthermore, it is also possible to use mixed sensor sets out of accelerometers and gyros. This case requires some decoupling conditions to avoid that some b_χ would appear in equation (35) and in (31) leading to a duplicate in the state vector.

$$\operatorname{curl} \mathbf{s}_\chi(\bar{\mathbf{r}}_{j_\Omega}) = \mathbf{0} \qquad \text{with} \quad \chi = 1, \dots, \Gamma_a \,, \tag{36}$$

$$\mathbf{s}_\chi(\bar{\mathbf{r}}_{j_a}) = \mathbf{0} \qquad \text{with} \quad \chi = 1+\Gamma_a, \dots, \Gamma_a + \Gamma_\Omega \,. \tag{37}$$

Additionally, the numbers Γ_a and Γ_Ω as well as the determination of the deformation modes $\mathbf{s}_\chi$ depend on the structure, the relevant motion excitation and on the accuracy to be achieved. Aspects of this statement will be illustrated in the following.

3.3 Aiding Model

Satellite navigation antennas are typically used as aiding devices in integrated navigation systems. In general, typical aiding principles use distance and velocity measurements to well-known points, not only radar, but also e.g. laser and ultrasonic units. The kinematical models in this case are quite simple, just using the geometry of the specific structure (see examples in section 3.4 and 3.6).

Apart from satellite navigation antennas or radar units, further structural sensors such as strain gauges, piezo ceramics or fibre optics can represent signal sources, which specially detect structural distortions. In this case, the aiding model is only a function of the additional degrees of freedom b_χ (see examples in section 3.4 and 3.6). The structural based, so called "internal aiding", is especially suitable to provide the observability of all additional state variables. Additionally, strain gauges are very reliable and favourably priced sensors. Thus, an internal aiding either can improve the performance of the integrated system on a low-cost basis or enables e.g. a reduction of the necessary number of satellite navigation antennas without violating the conditions of observability.

3.4 Example of a Sensor Set with Three Peripheral Accelerometers

The theory of modelling flexible structures is demonstrated by the example mentioned above using three accelerometers as peripheral sensors (Figure 6). The structure consists of a beam of length l and constant thickness h. Like the rigid multibody example in section 2.4 one end slides on a rail and is connected to a wall with a spring. Representing the IMU, two accelerometers and one gyro are fixed to the bar at the swivel joint and generate the signals u_1, u_2 (linear accelerations), u_6 (angular rate), and u_7 (angular acceleration). In addition, three peripheral accelerometers (u_3, u_4, u_5) supply input signals, and three unit deformations $\mathbf{s}_\chi$, $\chi = 1, 2, 3$ are considered to describe the elastic displacement of the structure. The aiding consists of four radar units measuring the distances ρ and velocities $\dot{\rho}$ (using Doppler shifts). Furthermore, strain gauges provide three aiding strain signals ε. The state $\mathbf{x}$ can be assembled into a 15 component vector containing the IMU motion components and the deformation variables b_χ. Furthermore $\mathbf{x}$ is extended by all biases Δu of the input sensors. This expansion is a typical measure to enhance the performance of integrated navigation systems (Farrell and Barth (1999)).

$$\begin{aligned} \mathbf{x} &= \begin{bmatrix} d & \dot{d} & \psi & b_1 & b_2 & b_3 & \dot{b}_1 & \dot{b}_2 & \dot{b}_3 & \Delta u_1 & \Delta u_2 & \Delta u_3 & \Delta u_4 & \Delta u_5 & \Delta u_6 \end{bmatrix}^T \\ &= \begin{bmatrix} x_1 & \dots & x_{15} \end{bmatrix}^T \end{aligned} \tag{38}$$

The input vector $\mathbf{u}$ contains the above mentioned seven components, that is five accelerometer inputs $u_1, \dots, u_5$ and one gyro measuring the angular velocity u_6 and its time derivative $u_7 = \dot{u}_6$.

$$\mathbf{u} = \begin{bmatrix} u_1 & u_2 & u_3 & u_4 & u_5 & u_6 & u_7 \end{bmatrix}^T \tag{39}$$

The actual component u_i can be modelled as a function of the measurement reading $\tilde{u}_i$, bias Δu_i, and noise w_{u_i}. The bias Δu_6 shall be a constant value, thus Δu_7 of the angular acceleration can be assumed to be zero. Therefore, the quantity Δu_7 does not appear in the state vector $\mathbf{x}$.

$$u_i = \tilde{u}_i + \Delta u_i + w_{u_i} \tag{40}$$
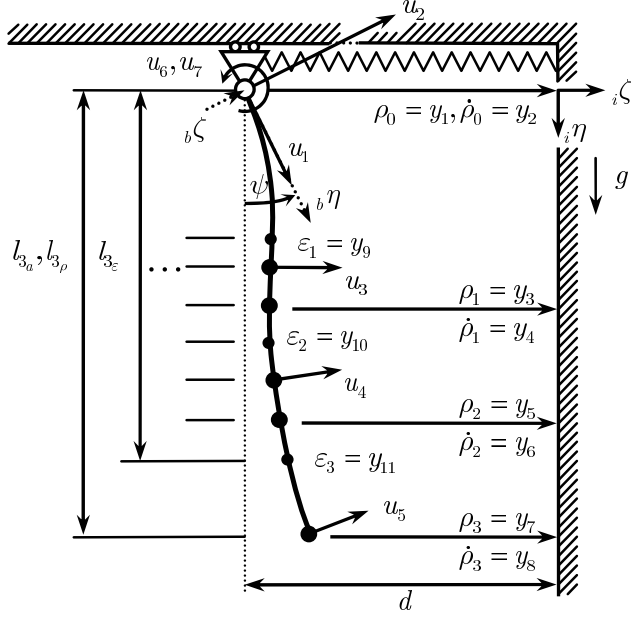
Figure 6: Elastic pendulum with three peripheral accelerometers.

Using moreover especially equations of section 3.1, the kinematical model of the beam (see equation (1)) can be written as the following:

$$
\mathbf{f}(\mathbf{x}, \mathbf{u}) =
\begin{bmatrix}
x_2 \\
(\tilde{u}_1 + x_{10}) \sin x_3 + (\tilde{u}_2 + x_{11}) \cos x_3 \\
\tilde{u}_6 + x_{15} \\
x_7 \\
x_8 \\
x_9 \\
\ddot{b}_1 (x_4, \ldots, x_{15}) \\
\ddot{b}_2 (x_4, \ldots, x_{15}) \\
\ddot{b}_3 (x_4, \ldots, x_{15}) \\
\{\mathbf{0}\}_{6 \times 1}
\end{bmatrix} .
\tag{41}
$$

The abbreviated expressions of $\ddot{b}_1 = \dot{x}_7$, $\ddot{b}_2 = \dot{x}_8$, and $\ddot{b}_3 = \dot{x}_9$ are formulated using equation (30)). Equation (40) has to be used to substitute the components u_i, which include also components of the state vector $(x_{10}, \ldots, x_{15})$. The matrix $_{j_ab}\mathbf{T}$ (see equation (30) and (31)) is the transformation between the body fixed and the sensor fixed coordinate system and is needed to arrange the expressions $\ddot{b}_\chi$. The first column belongs to the η component, the second to the χ component and the third one describes the rotational component.

$$
_{j_ab}\mathbf{T} =
\begin{bmatrix}
\cos\left(\arctan\left(\alpha_{j_a}\right)\right) & -\sin\left(\arctan\left(\alpha_{j_a}\right)\right) & 0 \\
\sin\left(\arctan\left(\alpha_{j_a}\right)\right) & \cos\left(\arctan\left(\alpha_{j_a}\right)\right) & 0 \\
0 & 0 & 1
\end{bmatrix}
=
\begin{bmatrix}
\frac{1}{\sqrt{1+\alpha_{j_a}^2}} & \frac{-\alpha_{j_a}}{\sqrt{1+\alpha_{j_a}^2}} & 0 \\
\frac{\alpha_{j_a}}{\sqrt{1+\alpha_{j_a}^2}} & \frac{1}{\sqrt{1+\alpha_{j_a}^2}} & 0 \\
0 & 0 & 1
\end{bmatrix}
\tag{42}
$$

With α_{j_a} containing the state variables x_4, x_5, x_6:

$$
\alpha_{j_a} = -\left(x_4 \cdot \frac{\partial s_1}{\partial_b \eta}\bigg|_{b\eta = l_{j_a}} + x_5 \cdot \frac{\partial s_2}{\partial_b \eta}\bigg|_{b\eta = l_{j_a}} + x_6 \cdot \frac{\partial s_3}{\partial_b \eta}\bigg|_{b\eta = l_{j_a}} \right) .
\tag{43}
$$

The following expression is directly obtained solving equation (30) for $\ddot{b}_\chi$ (using the χ component of the vector equation):

$$
\begin{bmatrix} \ddot{b}_1 \\ \ddot{b}_2 \\ \ddot{b}_3 \end{bmatrix} = \begin{bmatrix} s_{1,1_a} & s_{2,1_a} & s_{3,1_a} \\ s_{1,2_a} & s_{2,2_a} & s_{3,2_a} \\ s_{1,3_a} & s_{2,3_a} & s_{3,3_a} \end{bmatrix}^{-1}
\tag{44}
$$

$$
\cdot \begin{bmatrix} -\alpha_{1_a}\left(2(\tilde{u}_6 + x_{15})\sum_{\chi=1}^{3}\dot{b}_\chi s_{\chi,1_a} + \tilde{u}_7\sum_{\chi=1}^{3}b_\chi s_{\chi,1_a} + (\tilde{u}_6+x_{15})^2 l_{1_a} - (\tilde{u}_1+x_{10})\right) \\ +(\tilde{u}_6+x_{15})^2\sum_{\chi=1}^{3}b_\chi s_{\chi,1_a} - \tilde{u}_7 l_{1_a} - (\tilde{u}_2+x_{11}) + (\tilde{u}_3+x_{12})\cdot\sqrt{1+\alpha_{1_a}^2} \\[2ex] -\alpha_{2_a}\left(2(\tilde{u}_6 + x_{15})\sum_{\chi=1}^{3}\dot{b}_\chi s_{\chi,2_a} + \tilde{u}_7\sum_{\chi=1}^{3}b_\chi s_{\chi,2_a} + (\tilde{u}_6+x_{15})^2 l_{2_a} - (\tilde{u}_1+x_{10})\right) \\ +(\tilde{u}_6+x_{15})^2\sum_{\chi=1}^{3}b_\chi s_{\chi,2_a} - \tilde{u}_7 l_{2_a} - (\tilde{u}_2+x_{11}) + (\tilde{u}_4+x_{13})\cdot\sqrt{1+\alpha_{2_a}^2} \\[2ex] -\alpha_{3_a}\left(2(\tilde{u}_6 + x_{15})\sum_{\chi=1}^{3}\dot{b}_\chi s_{\chi,3_a} + \tilde{u}_7\sum_{\chi=1}^{3}b_\chi s_{\chi,3_a} + (\tilde{u}_6+x_{15})^2 l_{3_a} - (\tilde{u}_1+x_{10})\right) \\ +(\tilde{u}_6+x_{15})^2\sum_{\chi=1}^{3}b_\chi s_{\chi,3_a} - \tilde{u}_7 l_{3_a} - (\tilde{u}_2+x_{11}) + (\tilde{u}_5+x_{14})\cdot\sqrt{1+\alpha_{3_a}^2} \end{bmatrix} .
$$

The inversion of the matrix formed solely by the unit deformations s_{χ,j_a} is assumed to be constant and has just to be calculated once before the Kalman filter initialisation. Chapter 4 will focus on the quantities s_{χ,j_a} in detail. In this case, the matrix composed solely of the unit deformations is quadratic because $\nu_a = \Gamma_a = 3$. (If $\nu_a > \Gamma_a$, this matrix is not quadratic anymore. Here, the pseudo-inverse of the rectangular matrix can be used following the Least Squares method.)

In order to complete the motion model, the compensation of the noise of the input $\mathbf{u}$ must be considered. Vector $\mathbf{w}$ includes therefore noise terms w_{u_i} describing the noise of $\mathbf{u}$ and additional terms $w_{\Delta\dot{u}_i}$ representing the noise of the time derivative of the bias Δu_i. Since Δu_7 is omitted in the state model, there is no need to introduce $w_{\Delta\dot{u}_7}$.

$$
\begin{aligned}
\mathbf{w} &= \begin{bmatrix} w_{u_1} & w_{u_2} & w_{u_3} & w_{u_4} & w_{u_5} & w_{u_6} & w_{u_7} & w_{\Delta\dot{u}_1} & w_{\Delta\dot{u}_2} & w_{\Delta\dot{u}_3} & w_{\Delta\dot{u}_4} & w_{\Delta\dot{u}_5} & w_{\Delta\dot{u}_6} \end{bmatrix}^T \\
&= \begin{bmatrix} w_1 & \dots & w_{13} \end{bmatrix}^T
\end{aligned}
\tag{45}
$$

The quadratic term $(\tilde{u}_6 + \Delta u_6 + w_{u_6})^2$ has to be linearised with respect to w_{u_6} in order to obtain the desired form of $\mathbf{G}\cdot\mathbf{w}$. This approximation is acceptable, because $|w_{u_6}|$ is typically small compared to the maximum of $|u_6|$. Accordingly, the 15×13 matrix $\mathbf{G}(\mathbf{x},\mathbf{u})$ can be arranged as follows.

$$
\mathbf{G} = \begin{bmatrix} 0 & 0 & 0 & 0 & 0 & 0 & 0 & \\ \sin(x_3) & \cos(x_3) & 0 & 0 & 0 & 0 & 0 & \{\mathbf{0}\}_{3\times6} \\ 0 & 0 & 0 & 0 & 0 & 1 & 0 & \\ & & \{\mathbf{0}\}_{3\times7} & & & & & \{\mathbf{0}\}_{3\times6} \\ \left\{ \begin{bmatrix} s_{1,1_a} & s_{2,1_a} & s_{3,1_a} \\ s_{1,2_a} & s_{2,2_a} & s_{3,2_a} \\ s_{1,3_a} & s_{2,3_a} & s_{3,3_a} \end{bmatrix}^{-1} \cdot \mathbf{L} \right\}_{3\times7} & & & & & & & \{\mathbf{0}\}_{3\times6} \\ & & \{\mathbf{0}\}_{6\times7} & & & & & \{\mathbf{I}\}_{6\times6} \end{bmatrix}
\tag{46}
$$

The $\mathbf{L}$ matrix is introduced as an intermediate step to gather $\mathbf{G}$

$$
\mathbf{L} = \begin{bmatrix} \alpha_{1_a} & -1 & \sqrt{1+\alpha_{1_a}^2} & 0 & 0 & \kappa_1 & (\alpha_{1_a}\cdot\sum_{\chi=1}^{3}b_\chi s_{\chi,1_a} - l_{1_a}) \\ \alpha_{2_a} & -1 & 0 & \sqrt{1+\alpha_{2_a}^2} & 0 & \kappa_2 & (\alpha_{2_a}\cdot\sum_{\chi=1}^{3}b_\chi s_{\chi,2_a} - l_{2_a}) \\ \alpha_{3_a} & -1 & 0 & 0 & \sqrt{1+\alpha_{3_a}^2} & \kappa_3 & (\alpha_{3_a}\cdot\sum_{\chi=1}^{3}b_\chi s_{\chi,3_a} - l_{3_a}) \end{bmatrix}
\tag{47}
$$

with $j = 1, 2, 3$ the expression for κ_j can be added to $\mathbf{L}$.

$$
\kappa_j = -\alpha_{j_a}\left(2\sum_{\chi=1}^{3}\dot{b}_\chi s_{\chi,j_a} + 2(\tilde{u}_6+x_{15})l_{j_a}\right) + 2(\tilde{u}_6+x_{15})\sum_{\chi=1}^{3}b_\chi s_{\chi,j_a}
\tag{48}
$$

Turning to the aiding signal, it consists of eleven signals as shown in Figure (6).

$$
\begin{aligned}
\mathbf{y} &= \begin{bmatrix} \rho_0 & \dot{\rho}_0 & \rho_1 & \dot{\rho}_1 & \rho_2 & \dot{\rho}_2 & \rho_3 & \dot{\rho}_3 & \varepsilon_1 & \varepsilon_2 & \varepsilon_3 \end{bmatrix}^T \\
&= \begin{bmatrix} y_1 & \cdots & y_{11} \end{bmatrix}^T
\end{aligned} \tag{49}
$$

The next steps will show the assembling of the vector $\mathbf{h}$ using the results from section 3.3. The theory of bending elastic beams is needed to process the measured strain ε (Roark and Young (1986)). The relation between the strain ε and flexure $\bar{w}$ is the following with W being the bending section modulus and I the geometrical moment of inertia.

$$
\frac{d^2 \bar{w}(_b\eta)}{d_b\eta^2} = -\frac{W}{I} \cdot \varepsilon(_b\eta) \tag{50}
$$

Furthermore, the introduction of auxiliary functions ν_k, $\dot{\nu}_k$ with $k = 0, 1, 2, 3$ and the unit bending curvature s''_χ with respect to the structural coordinate $_b\eta$ is suitable.

$$
\nu_k = x_4 \cdot s_1(l_{k_\rho}) + x_5 \cdot s_2(l_{k_\rho}) + x_6 \cdot s_3(l_{k_\rho}) \,, \tag{51}
$$

$$
\dot{\nu}_k = x_7 \cdot s_1(l_{k_\rho}) + x_8 \cdot s_2(l_{k_\rho}) + x_9 \cdot s_3(l_{k_\rho}) \,, \tag{52}
$$

$$
s''_\chi(l_{m_\varepsilon}) = \left. \frac{d^2 s_\chi}{d_b\eta^2} \right|_{_b\eta = l_{m_\varepsilon}} , \quad m = 1, 2, 3 \,. \tag{53}
$$

The aiding model can now be written for a rectangular beam section with h being the thickness of the beam:

$$
\mathbf{h}(\mathbf{x}, \mathbf{u}) = \begin{bmatrix}
x_1 \\
x_2 \\
x_1 + l_{1_\rho} \sin(x_3) + \nu_1 \cos(x_3) \\
x_2 + (\tilde{u}_6 + x_{15}) \cdot (l_{1_\rho} \sin(x_3) + \nu_1 \cos(x_3)) + \dot{\nu}_1 \cos(x_3) \\
x_1 + l_{2_\rho} \sin(x_3) + \nu_2 \cos(x_3) \\
x_2 + (\tilde{u}_6 + x_{15}) \cdot (l_{2_\rho} \sin(x_3) + \nu_2 \cos(x_3)) + \dot{\nu}_2 \cos(x_3) \\
x_1 + l_{3_\rho} \sin(x_3) + \nu_3 \cos(x_3) \\
x_2 + (\tilde{u}_6 + x_{15}) \cdot (l_{3_\rho} \sin(x_3) + \nu_3 \cos(x_3)) + \dot{\nu}_3 \cos(x_3) \\
-\frac{h}{2} (x_4 \cdot s''_1(l_{1_\varepsilon}) + x_5 \cdot s''_2(l_{1_\varepsilon}) + x_6 \cdot s''_3(l_{1_\varepsilon})) \\
-\frac{h}{2} (x_4 \cdot s''_1(l_{2_\varepsilon}) + x_5 \cdot s''_2(l_{2_\varepsilon}) + x_6 \cdot s''_3(l_{2_\varepsilon})) \\
-\frac{h}{2} (x_4 \cdot s''_1(l_{3_\varepsilon}) + x_5 \cdot s''_2(l_{3_\varepsilon}) + x_6 \cdot s''_3(l_{3_\varepsilon}))
\end{bmatrix} . \tag{54}
$$

Like the aiding model in section 2.4 the vector $\mathbf{h}$ is a function of the input $\mathbf{u}$ which contravenes the Kalman filter theory. However, this fact is commonly accepted in practice. The same is true for the circumstance, that the sensor noise, i.e. w_1 to w_{13}, v_1 to v_{11} is not white (equations (6), (7), Farrell and Barth (1999), Wagner (2003)).

The choice of sensors and their positioning $(l_{j_a}, l_{k_\rho}, l_{m_\varepsilon})$ along the beam is significant for the filter performance. Section 4.3 will treat the appropriate positioning and optimisation of sensors.

Using equation (17), the aspect of observability was investigated (compare Wagner (2003)). The presented model shows not observable state variables in particular Δu_1. Nevertheless, the model can be easily changed into a completely observable system as shown in section 3.5. The additional naming "completely observable" shall clarify that the system guarantees the observability without considering the type of dynamic excitation. In contrast to this property a "weakly observalble" system (Dambeck (1995)) can become unobservable if it is not sufficiently excited by $\mathbf{u}$. This type typically occurs for integrating an inertial navigation system with a single antenna GPS receiver.

3.5 Further Models using Accelerometers as Peripheral Sensors

The previous example of modelling flexible continuum is meant to be an example to explain the procedure in general. The aspect of observability shows that models have to be developed that fulfill the requirement of section 2.3 to maintain the stability of the filter algorithm.

Expanding the state vector of equation (38) with the vertical distance of the slide $d_v = x_{16}$ and its vertical velocity $\dot{d}_v = x_{17}$ yields a completely observable system.

$$
\dot{d}_v = x_{17} \,, \tag{55}
$$

$$
\ddot{d}_v = (\tilde{u}_1 + x_{10}) \cos x_3 - (\tilde{u}_2 + x_{11}) \sin x_3 + g \,. \tag{56}
$$

Obviously, the new quantities are equal to zero because of the vertical fixation of the slide. These two informations are used in the aiding model.

$$y_{12} = \dot{d}_v + v_{12} = 0, \quad h_{12} = x_{16}, \tag{57}$$

$$y_{13} = \ddot{d}_v + v_{13} = 0, \quad h_{13} = x_{17}. \tag{58}$$

The term $\mathbf{G} \cdot \mathbf{w}$ must be extended as well as $\mathbf{f}$, $\mathbf{h}$, and the Jacobians $\mathbf{F}$, $\mathbf{H}$ by two lines.

A second possibility forgoes the accelerometer u_1. The motion model differs from the model in section 3.4 in the following

$$\dot{x}_3 = \dot{d} = \frac{\tilde{u}_2 + x_{11}}{\cos x_3} \tag{59}$$

and additionally the terms $\ddot{b}_\chi$, $\mathbf{G} \cdot \mathbf{w}$, and $\mathbf{F}$ are different, too. The disadvantage of this model is the numerical problem for $|\psi| \approx 90°$. Again, all the kinematical models presented in this chapter are completely observable and show better stability performance compared to the model of section 3.4.

Models including two, three and four additional degrees of freedom b_χ have been developed and compared. However, beforehand the device of the function s_χ has to be explained. The results will be presented later on in chapter 5 utilising the extensions of equations (55) to (58) for the models with peripheral accelerometers.

3.6 Example of a Sensor Set with Three Peripheral Gyros

This section will show the kinematical model of Figure 7 using three gyros as peripheral sensors. The structure consists like the example above of a beam of length l and constant thickness h. The restraints of this model are the same as in the example of section 3.4. Representing the IMU, two accelerometers and one gyro are fixed to the bar at the swivel joint and generate the signals u_1, u_2 (linear accelerations), u_3 (angular rate). Three peripheral gyros (u_4, u_5, u_6) supply input signals, and three unit deformations $\mathbf{s}_\chi$, $\chi = 1, 2, 3$ are considered to describe the elastic displacement of the structure. The aiding consists of four radar units measuring the distances ρ. Finally, strain gauges provide three internal aiding signals ε. The state $\mathbf{x}$ can be assembled into a 12 component vector which is again expanded with the bias Δu of all input sensors:

$$\begin{aligned}
\mathbf{x} &= \begin{bmatrix} d & \dot{d} & \psi & b_1 & b_2 & b_3 & \Delta u_1 & \Delta u_2 & \Delta u_3 & \Delta u_4 & \Delta u_5 & \Delta u_6 \end{bmatrix}^T \\
&= \begin{bmatrix} x_1 & \dots & x_{12} \end{bmatrix}^T.
\end{aligned} \tag{60}$$

The input $\mathbf{u}$ contains in this case six components, because the time derivative of the angular velocity is of no need:

$$\mathbf{u} = \begin{bmatrix} u_1 & u_2 & u_3 & u_4 & u_5 & u_6 \end{bmatrix}^T. \tag{61}$$

Following equation of section 3.2, the kinematical model of the beam can be assembled as follows.

$$\mathbf{f}(\mathbf{x}, \mathbf{u}) = \begin{bmatrix} x_2 \\ (\tilde{u}_1 + x_7)\sin x_3 + (\tilde{u}_2 + x_8)\cos x_3 \\ \tilde{u}_3 + x_9 \\ \dot{b}_1(x_9, x_{10}, x_{11}, x_{12}) \\ \dot{b}_2(x_9, x_{10}, x_{11}, x_{12}) \\ \dot{b}_3(x_9, x_{10}, x_{11}, x_{12}) \\ \{\mathbf{0}\}_{6 \times 1} \end{bmatrix} \tag{62}$$

In this case, the transformation matrix is $_{j_\Omega b}\mathbf{T} = {}_{j_a b}\mathbf{T}$ (see equation (42)). The abbreviated expressions of $\dot{b}_1 = \dot{x}_4$, $\dot{b}_2 = \dot{x}_5$, and $\dot{b}_3 = \dot{x}_6$ follow equation (34) to (35), just using the third component of this vector equation. Here, the transformation matrix has no effect on the rotational component of the vector equation which simplifies the model significantly compared to the models using accelerometers as peripheral sensors.

$$\begin{bmatrix} \dot{b}_1 \\ \dot{b}_2 \\ \dot{b}_3 \end{bmatrix} = - \underbrace{\begin{bmatrix} s'_{1,1\Omega} & s'_{2,1\Omega} & s'_{3,1\Omega} \\ s'_{1,2\Omega} & s'_{2,2\Omega} & s'_{3,2\Omega} \\ s'_{1,3\Omega} & s'_{2,3\Omega} & s'_{3,3\Omega} \end{bmatrix}^{-1}}_{\mathbf{S}_\Omega^*} \cdot \begin{bmatrix} (\tilde{u}_4 + x_{10}) - (\tilde{u}_3 + x_9) \\ (\tilde{u}_5 + x_{11}) - (\tilde{u}_3 + x_9) \\ (\tilde{u}_6 + x_{12}) - (\tilde{u}_3 + x_9) \end{bmatrix} \quad \text{with } s'_{\chi, j_\Omega} = \left. \frac{\partial s_\chi}{\partial_b \eta} \right|_{b\eta = l_{j_\Omega}} \tag{63}$$

In this case, vector $\mathbf{w}$ is composed out of 12 components that compensate the noise of the input $\mathbf{u}$:

$$\begin{aligned}
\mathbf{w} &= \begin{bmatrix} w_{u_1} & w_{u_2} & w_{u_3} & w_{u_4} & w_{u_5} & w_{u_6} & w_{\Delta \dot{u}_1} & w_{\Delta \dot{u}_2} & w_{\Delta \dot{u}_3} & w_{\Delta \dot{u}_4} & w_{\Delta \dot{u}_5} & w_{\Delta \dot{u}_6} \end{bmatrix}^T \\
&= \begin{bmatrix} w_1 & \dots & w_{12} \end{bmatrix}^T.
\end{aligned} \tag{64}$$

Figure 7: Elastic pendulum with three peripheral gyros.

Accordingly, the 12×12 matrix $\mathbf{G}(\mathbf{x}, \mathbf{u})$ can be arranged as follows.

$$
\mathbf{G} = \begin{bmatrix}
0 & 0 & 0 & 0 & 0 & 0 & \\
\sin(x_3) & \cos(x_3) & 0 & 0 & 0 & 0 & \{\mathbf{0}\}_{3\times 9} \\
0 & 0 & 1 & 0 & 0 & 0 & \\
& & \left\{ \mathbf{S}^*_\Omega \begin{bmatrix} -(\tilde{u}_3 + x_9) & \tilde{u}_4 + x_{10} & 0 & 0 \\ -(\tilde{u}_3 + x_9) & 0 & \tilde{u}_5 + x_{11} & 0 \\ -(\tilde{u}_3 + x_9) & 0 & 0 & \tilde{u}_6 + x_{12} \end{bmatrix} \right\}_{3\times 4} & \{\mathbf{0}\}_{3\times 6} \\
& & \{\mathbf{0}\}_{6\times 6} & & & & \{\mathbf{I}\}_{6\times 6}
\end{bmatrix}
\tag{65}
$$

The aiding signals are four distance measurements ρ_0 to ρ_3, velocity $\dot{\rho}_0$, and three strain measurements ε_1 to ε_3:

$$
\begin{aligned}
\mathbf{y} &= \begin{bmatrix} \rho_0 & \dot{\rho}_0 & \rho_1 & \rho_2 & \rho_3 & \varepsilon_1 & \varepsilon_2 & \varepsilon_3 \end{bmatrix}^T \\
&= \begin{bmatrix} y_1 & \cdots & y_8 \end{bmatrix}^T .
\end{aligned}
\tag{66}
$$

The resulting aiding model is in this case just a function of $\mathbf{x}$ which fulfills the Kalman filter prerequisites:

$$
\mathbf{h}(\mathbf{x}) = \begin{bmatrix}
x_1 \\
x_2 \\
x_1 + l_{1_\rho} \sin(x_3) + \left(x_4 \cdot s_1(l_{1_\rho}) + x_5 \cdot s_2(l_{1_\rho}) + x_6 \cdot s_3(l_{1_\rho}) \right) \cos(x_3) \\
x_1 + l_{2_\rho} \sin(x_3) + \left(x_4 \cdot s_1(l_{2_\rho}) + x_5 \cdot s_2(l_{2_\rho}) + x_6 \cdot s_3(l_{2_\rho}) \right) \cos(x_3) \\
x_1 + l_{3_\rho} \sin(x_3) + \left(x_4 \cdot s_1(l_{3_\rho}) + x_5 \cdot s_2(l_{3_\rho}) + x_6 \cdot s_3(l_{3_\rho}) \right) \cos(x_3) \\
-\frac{h}{2} \left(x_4 \cdot s_1''(l_{1_\varepsilon}) + x_5 \cdot s_2''(l_{1_\varepsilon}) + x_6 \cdot s_3''(l_{1_\varepsilon}) \right) \\
-\frac{h}{2} \left(x_4 \cdot s_1''(l_{2_\varepsilon}) + x_5 \cdot s_2''(l_{2_\varepsilon}) + x_6 \cdot s_3''(l_{2_\varepsilon}) \right) \\
-\frac{h}{2} \left(x_4 \cdot s_1''(l_{3_\varepsilon}) + x_5 \cdot s_2''(l_{3_\varepsilon}) + x_6 \cdot s_3''(l_{3_\varepsilon}) \right)
\end{bmatrix} .
\tag{67}
$$

4 Model Reduction

The dimensions of the beam in Figure 8 were chosen to fit approximately the first natural frequency of a wing of a large aircraft. In order to describe the real structure with the kinematical model presented above we need to simplify a detailed structural model. There are several methods available to do this, like Balanced Realisation and Krylov subspace method just to name a few (Lohmann and Salimbahrami (2004)).

106

Figure 8: Model reduction of the beam structure.

In this article the modal approach will be discussed considering the most important vibration modes. First, two dimensional Finite Euler-Bernoulli beam elements have been chosen to describe the real structure and an additional lumped mass has been used to describe e.g. the mass of the slide (Figure 8 on the right), other masses can be added if necessary. The Euler-Bernoulli beam elements employed use cubic interpolation functions, which make them reasonably accurate for cases involving distributed loading along the beam. Therefore, they are well suited for dynamic vibration studies, where the d'Alembert forces provide such distributed loading. These elements are intended for small-strain, large-rotation analysis using a consistent mass formulation.

There are three reasons for using the model: the first is to obtain detailed simulated motion data of the vibrating structure including the measurements $\mathbf{u}$ and $\mathbf{y}$. Furthermore, the simulation described in section 4.2 is meant to prepare the real experiment on the real beam structure, which will be realised in the near future. The third purpose is to obtain the important eigenmodes of the system which will partially be used as unit deformations $\mathbf{s}_{\chi,j_a}$.

4.1 Modal Analysis

In the following a linear modal analysis is performed with the system in Figure 8 to obtain its natural frequencies and the natural modes. The left picture of Figure 9 shows the first four elastic modes and the rigid body mode which is due to the pivoted upper end (1. node) of the beam. As expected, the first elastic eigenmode shows one zero-crossing, the second elastic eigenmode two zero-crossings and so on. These normalised eigenmodes are obtained with respect to the inertial coordinate system index i. However, due to the theory given above the obtained eigenmodes have first to be transformed into the body coordinate system. The transformed normalised eigenmodes are shown on the right side of Figure 9.

The first and second transformed eigenmode, however, look similar. The first, third, and fourth eigenmodes are clearly to distinguish. Using these transformed eigenmodes as sources of s_{χ,j_a} leads to bad estimation results and possibly to an unstable system. This is due to the similar shapes of the first and second transformed eigenmode. The filter is hardly able to distinguish between the first and second eigenform. Therefore the modes are combined in a so-called mixed mode, that is the average displacement value of both eigenmodes.

For instance, in section 3.4 a three deformation variable model was presented. In this case the mixed, third, and fourth eigenmodes are used as unit deformations. Exemplarily, the value of $s_{1,3_a}$ can be determined regarding $\chi = 1$ that means the first unit deformation, being here the mixed eigenmode. The next information $j_a = 3_a$ indicates that the third peripheral accelerometer is considered, which is placed at the lowest point (node 31) at $l = 4$ m. This yields using Figure 9 at the right side a value $s_{1,3_a} = 1$. Furthermore, the values of $\frac{\partial s_\chi}{\partial_b \eta}$ and $\frac{d^2 s_\chi}{d_b \eta^2}$ are obtained by differentiating the transformed eigenmode shapes (Figure 10).
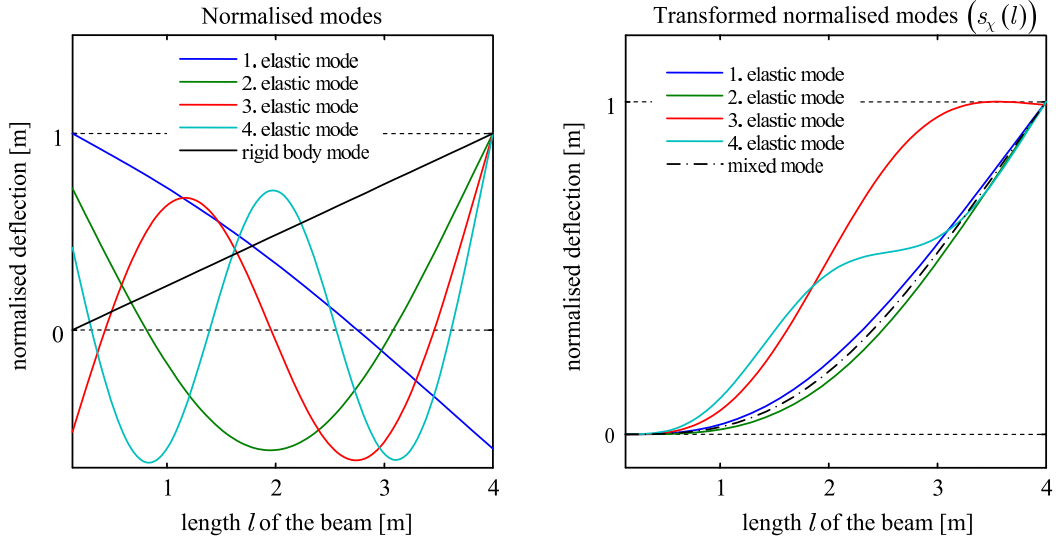
Figure 9: Eigenmodes and transformed elastic mode shapes.
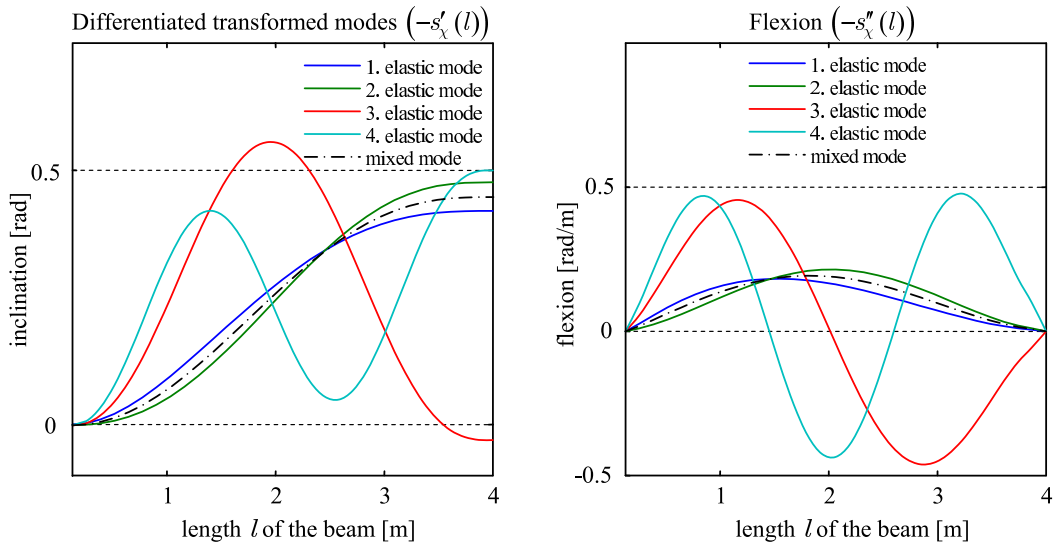
Figure 10: Inclination and flexion.

4.2 Data Simulation

The data for **u** and **y** as well as for the **x**-reference were generated by a geometrically nonlinear simulation using Rayleigh Damping and gravity. Data sets from 1000 to 1500s were produced with different kinds of excitation: The first one was an impulse-type excitation each hundred seconds which could be realised with strokes against the structure. Additionally, a second set of a sinusoidal excitation, for instance realised with a shaker, at the upper end of the beam was superimposed to the impulse-type excitation. The chosen forms of excitation are idealisations of an excited airplane during flight due to gusts. Having extracted the data out of the Finite Element model, the obtained data were falsified to simulate a real measurement device. First, to simulate an offset of the measurement device a constant bias was added to the signals of the accelerometers and gyros. Secondly, in order to simulate measurement noise, normal distributed random numbers with adjustable standard deviation were added to the obtained signals (signals of accelerometers, gyros, radar units and strain gauges).

4.3 Sensor Positioning

Sensor positioning is significant for filter performance because it determines the observability of the system. Placing for example three peripheral accelerometer of the example in section 3.4 tight together, would lead to similar

108

measurement results at the sensors. The distinction of the different eigenforms would be difficult, what could eventually cause a loss of observability. Even if the sensors are distributed along the structure they could still be placed at nodal points with no significant movement at all. The estimates of the deformation variables would be corrupt. In order to avoid the mentioned negative effects concerning filter stability, the peripheral accelerometers, peripheral gyros, radar units and strain gauges used in the examples of section 3.4 to 3.6 were positioned using the information of the eigenmodes of Figure 9 and Figure 10.

The peripheral accelerometers of the two mode model were positioned at node 15 and 24 (that is $l \approx 1.87$ m and 3.07 m). The additional accelerometer of the three mode model was located at $l = 4.0$ m (node 31). The four mode model had an additional accelerometer at $l \approx 1.33$ m (node 11). This positioning makes it possible to distinguish the deformation modes. The additional gyros of the three mode model of example 3.6 were placed at node 15, 20, and 31 (that is $l \approx 1.87$ m and 2.53 m, 4.0 m) using the information of maximal inclination.

The radar units were placed on the same nodes like the peripheral accelerometers and peripheral gyros respectively which is not coercively necessary. The three strain gauges were placed using the information of the maximal curvature of s_χ (Figure 10 on the right side). Thus, strain gauges of the two mode model were positioned at node 9 and 16 (that is $l \approx 1.07$ m and 2 m). The three mode models (using peripheral accelerometers and gyros) had an additional strain gauge at node 25 ($l = 3.2$ m). And finally, the four mode model had an additional strain gauge at node 5 ($l \approx 0.53$ m).

5 Simulated System Test

This chapter presents the simulation results of different kinematical models presented in section 3.4 to 3.6: In the following, the number of additional degrees of freedom b_χ will be discussed, as well as the estimates of the state vector $\mathbf{x}$ and their errors. Furthermore, a comparison between kinematical models using peripheral accelerometers and peripheral gyros is shown. As mentioned the reference values used for comparison were generated by simulation.

At first, a comparison of four different kinematical models is shown. The first model contains two additional degrees of freedom b_1, b_2, three additional degrees of freedom b_1, b_2, b_3 and the third one four additional degrees b_1 to b_4 using accelerometers as peripheral sensors. The kinematical model is of the same structure as the presented example of section 3.4 just to be adjusted by the specific number of b_χ. The fourth model uses three additional variables b_1 to b_3 utilising three gyros as peripheral sensors (see section 3.6).

Figure 11 shows the error of elastic deformation at the end of beam of the four models described above. The upper plot belongs to the first model including b_1, b_2 and so on. For this, it has to be noted additionally, that the vibrating beam showed in each case a maximum elastic deformation of almost 50 cm at the end of the beam which reaches the upper bound of the linear theory of the elastic modes.

The first three subplots show an abrupt rise of the error each hundred seconds. This is due to the impulse type excitation which takes place at these time steps. At these points, the excitation exceeds the linear theory of eigenmodes causing the worst estimation of motion. Moreover, the error of elastic deformation for a two mode model is higher than the error of the three mode model. The additional variable b_3 improves the estimates from an average error of 8 cm to about 6 cm. However, the fourth model using gyros as peripheral sensors shows much better estimation results. Indeed, the filter performance needs a few hundred seconds to reach a steady state behaviour, but the estimation error is about 2 cm which is significantly smaller than the models using peripheral accelerometers. A possible explanation of this effect is the fact that the additional variables b_χ using peripheral gyros have just to be integrated once. However, the models using accelerometers include two integration steps from $\ddot{b}_\chi$ to b_χ. This causes a tremendous increase of inaccuracy.

The third model using four accelerometers of Figure 11 does not show a better performance the three mode model. In this case, the estimation result of the error of elastic deformation shows an offset. The fourth elastic unit deformation is barely excited which causes a loss of observability of b_4.

A passing remark is given on the reference values of b_χ that have to be gained by an intermediate step using the information of position (η and χ component) of the considered node from the Finite Element program. The quantities b_χ of the presented modal approach imply that the motion of the beam is described using the linear theory of the eigenmodes. However, the simulation of the measurement signals were gained using a nonlinear analysis described in section 4.2. That means, the reference values of b_χ represent just a simplification of the nonlinear behaviour of the beam. Furthermore, the reference values of b_χ differ slightly depending on the nodes used to calculate b_χ. Nonetheless, the reference values of b_χ were checked at the same nodes like the position of the peripheral accelerometers to make the quantities b_χ comparable and meaningful.

The following plots use the kinematical model of the example in section 3.4 expanded with equations (55)-(58). This expansion of the example yields the best results of the presented further models of section 3.5 and will therefore be shown in the succeeding plots using a typical time sequence. Figure 12 displays the state variable d and its
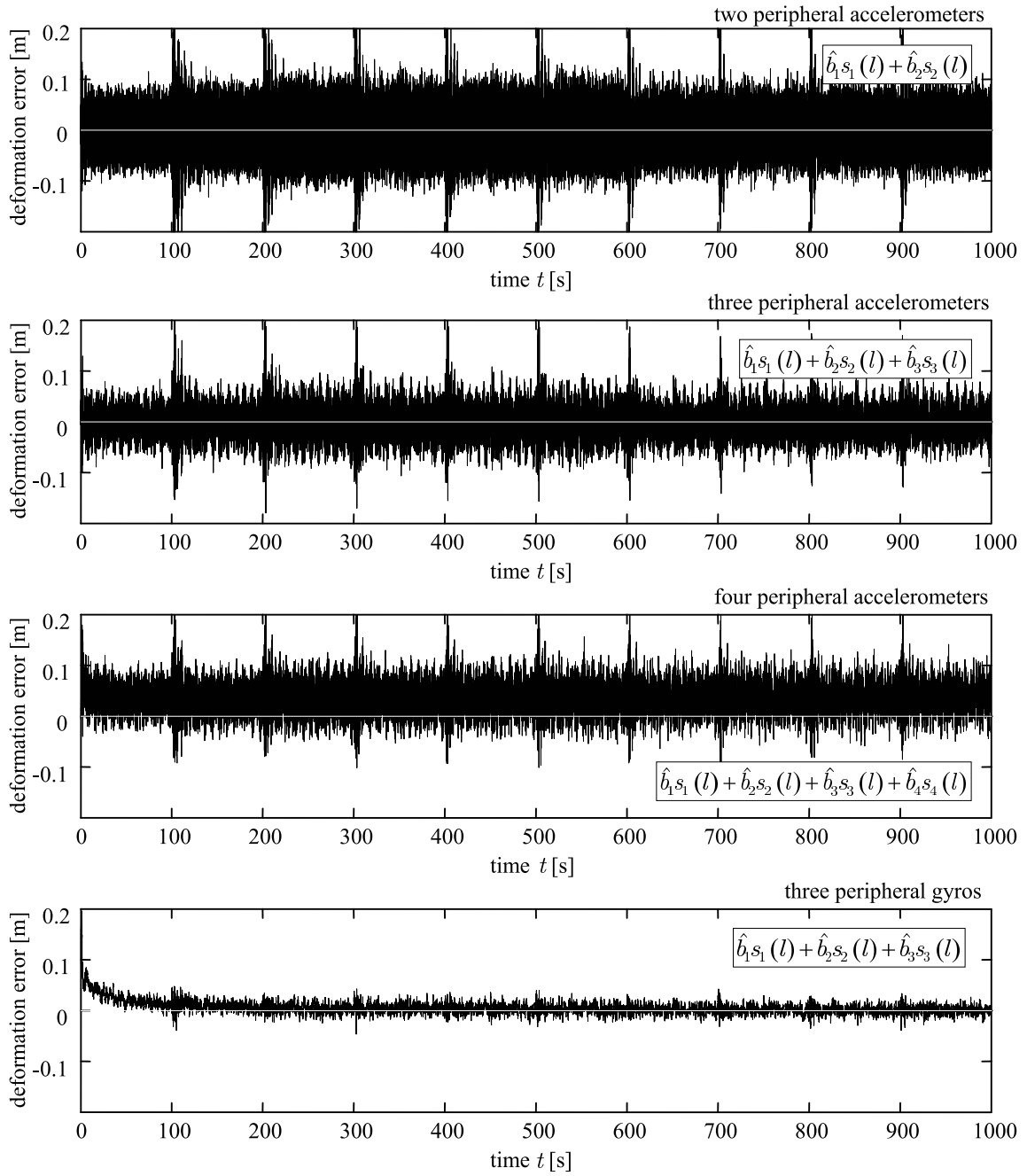
Figure 11: Estimation error of the elastic displacement $\sum \hat{b}_\chi s_\chi(l)$ at the end of the beam ($l = 4$ m) for different models including two, three and four deformation variables b_χ using two, three, four peripheral accelerometers or three peripheral gyros.

error. The maximal amplitude of the distance d to the nearby wall is approximately 25 cm and its average error is about 1 cm.

The angle ψ is displayed in Figure 13 with a maximum deflection of 12° and an average error of 0.3°.

Focusing on the deformation variables b_χ at Figure 14 the different frequencies of the oscillation are clearly to distinguish. These frequencies are due to the vibration generator frequencies of the sinusoidal excitation which in this specific case where chosen to fit approximately the eigenfrequencies of the system. This Figure shows the reference and estimate sampled at 100 Hz and the aiding measurements sampled at 10 Hz. Furthermore, the absolute errors of all b_χ are approximately of the same magnitude, however, the relative errors rise with increasing number of b_χ since $|b_1| > |b_2| > |b_3|$.

Finally, the biases $\Delta u_1, \ldots, \Delta u_6$ are plotted in Figure 15. The estimates of $\Delta u_6, \Delta u_1, \Delta u_2$ (bias of the input of the gyro and the accelerometers of the IMU) adapt quickly to the predefined offset. However, the biases of the peripheral accelerometers $\Delta u_3, \Delta u_4, \Delta u_5$ show a different behaviour; the convergence of the reference and

110
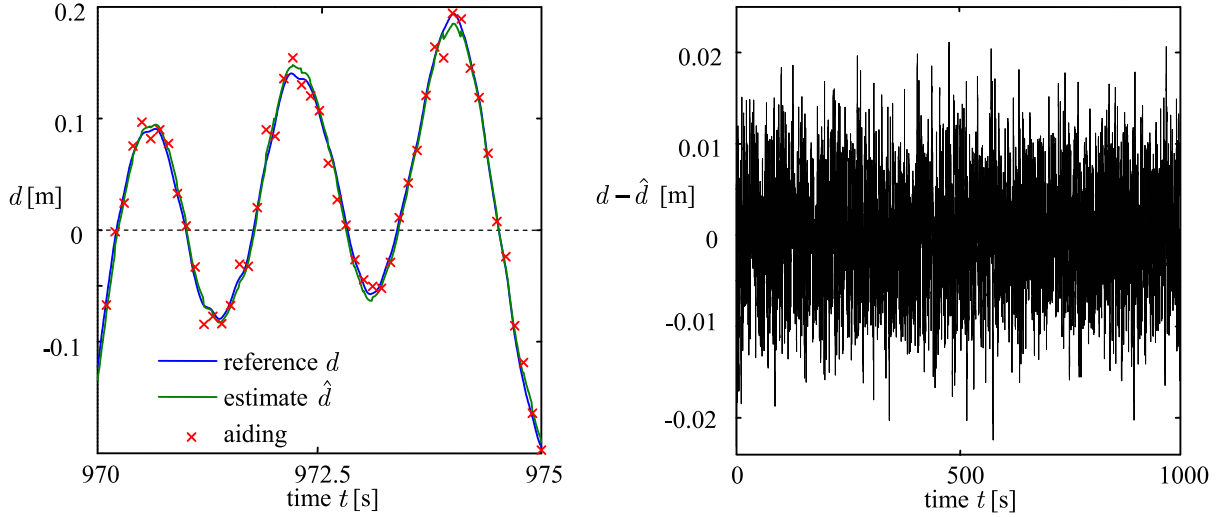
Figure 12: Distance d, estimate $\hat{d}$ and the error of distance $d - \hat{d}$ of the three mode model using three peripheral accelerometers.
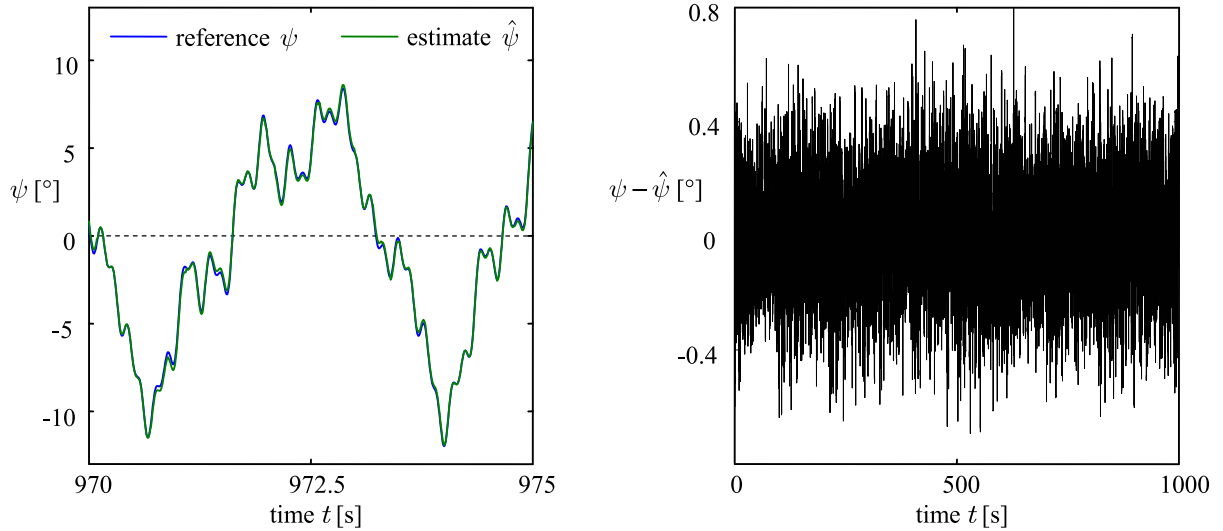
Figure 13: Angle ψ, estimate $\hat{\psi}$ and the error of angle $\psi - \hat{\psi}$ of the three mode model using three peripheral accelerometers.

the estimate cannot be shown within the first 1000 seconds of the simulation. But, the mismatch of the estimates among each other correspond. Additionally, the estimates of the bias tend towards their individual references.

6   Conlusions and Future Work

The principle of integrated navigation systems can be expanded to flexible vehicles with large structural dimensions in order to measure the flexure. The main role for the measurement system is a suitable kinematical model of the considered structure. Including deformation variables into this model, it is possible to describe the motion of flexible structures using acceleration, velocity, position, and strain. The filter algorithm produces smooth estimates of the desired motion and blends the noisy signals of the different measurement devices. This opens a new class of possibility for motion control of large structures and for structural monitoring (applications are gust alleviation, minimising structural loads of wings, and sound reduction of helicopter blades etc.).

The simulated system test in chapter 5 is meant to prepare the experimental verification of the presented measurement system. Moreover, more kinematical models including peripheral gyros and a combination of both peripheral sensor types (gyros and accelerometers) have to be developed and compared with models including solely peripheral accelerometers.

Besides the modal approach, including the mixed mode approximation, new methods to describe the flexibility of
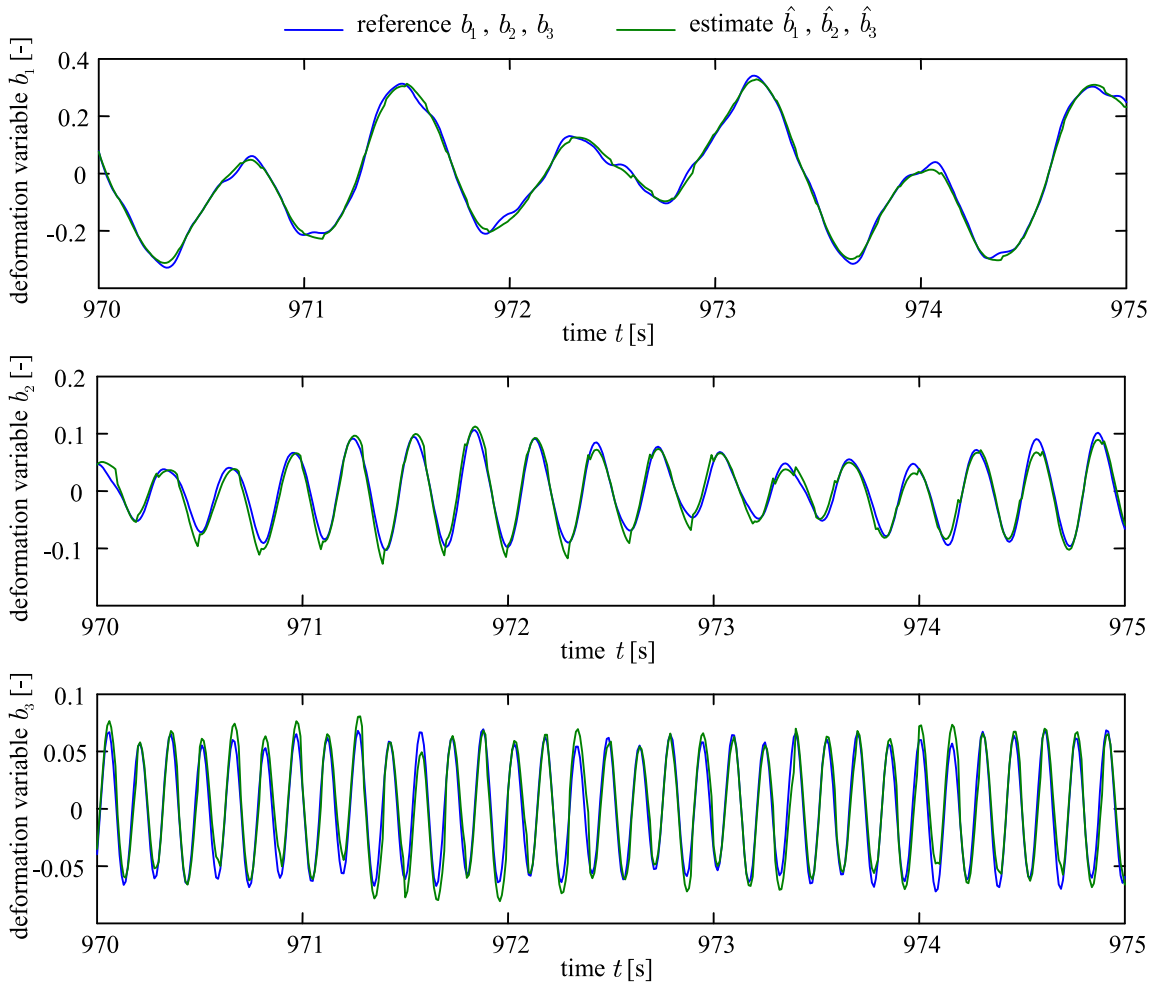
Figure 14: Deformation variables b_1, b_2 and b_3 using three peripheral accelerometers.

a structure have to be considered. The Krylov subspace method is such an approach that allows reducing very high order models with several ten thousands of state variables.

Sensor optimisation has to be investigated in detail including more parameters to be optimised. This includes on the one hand the choice of sensors, that means the question has to be investigated which sensors are favourable for a specific structure. On the other hand the position of the sensors along the structure has to be further optimised. So far, the information of the eigenmodes was used to position the sensors at points of maximal amplitude. Therefore, the reduced model of the beam with 31 nodes, which is sufficient for a first investigation, should be expanded.

Filter tuning is also important for filter performance and can be improved with new methods including dynamically tuned matrices (e.g. **Q** matrix). The use of several Kalman filters running in parallel using each different kinematical models has to be tested. These so-called cascadian filters (Sasiadek and Wang (2001)) could choose between different kinematical models including more or less deformation variables. The idea of switching the filter can be realised with an additional dynamic parameter. This paramater to be introduced judges the actual movement in terms of dominant vibration modes. The appropriate model using the optimal number of deformation variables can now be chosen to stabilise filter performance in different phases of excitation. This approach can furthermore be used for high safety applications with system redundancy requirements.
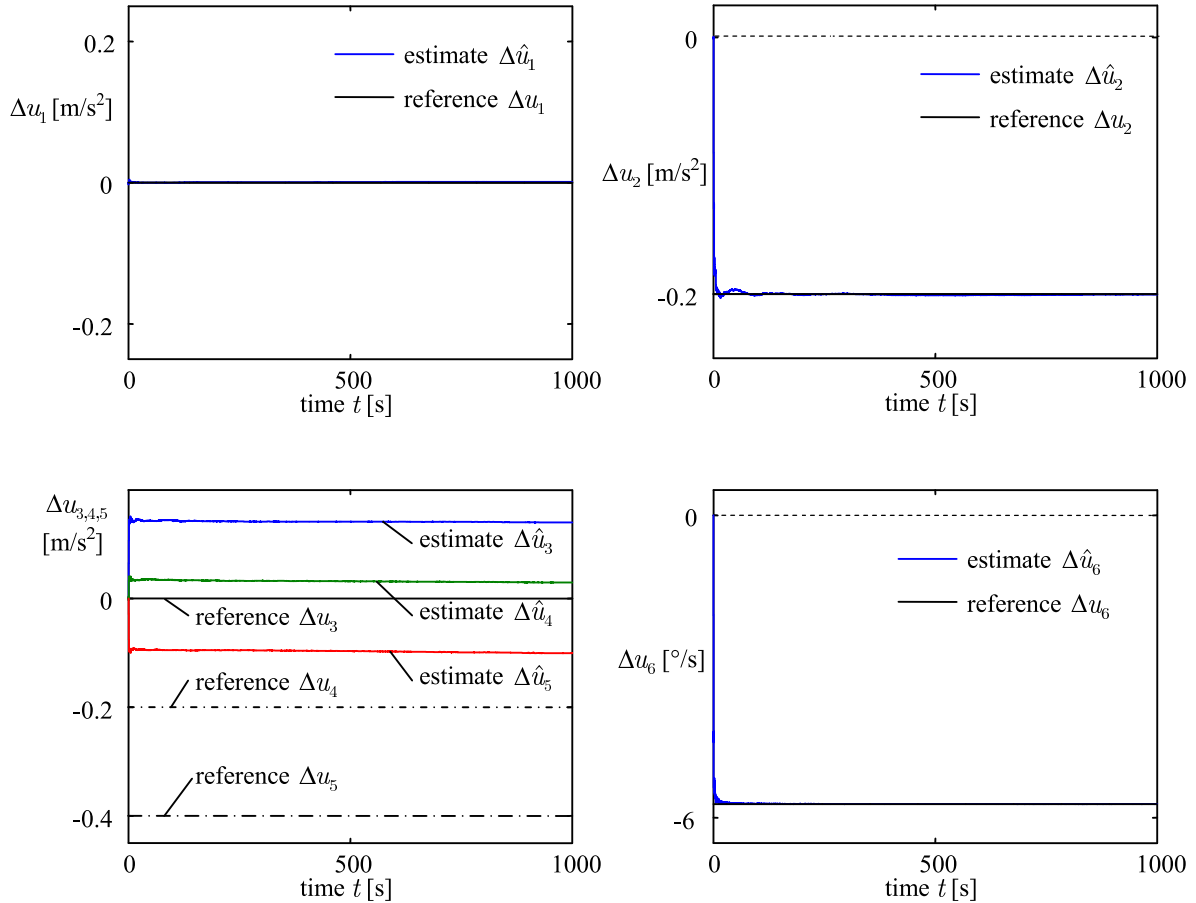
Figure 15: Bias Δu_1 to Δu_6 and their estimates $\Delta \hat{u}_1$ to $\Delta \hat{u}_6$ of the three mode model using three peripheral accelerometers.

References

Dambeck, J. H.: Observability and controllability analysis for a strapdown inertial navigation system. *High Precision Navigation 95*, (K. Linkwitz and U. Hangleiter), Ferd. Duemmler, Bonn, (1995), 149 – 158.

Farrell, J. A.; Barth, M.: *The Global Positioning System and Inertial Navigation*. McGraw-Hill, New York, et al. (1999).

Gelb, A.: *Applied Optimal Estimation*. The M.I.T. Press, Cambridge, MA, London (1989).

Lohmann, B.; Salimbahrami, B.: Ordnungsreduktion mittels Krylov-Unterraummethoden. *Automatisierungstechnik*, Oldenbourg Verlag 52, (2004), 30 – 38.

Quinn, P.; Lewis, D.; Berarducci, M.; Miller, M.: Precise estimation and compensation of antenna lever arm flexure using auxiliary inertial sensors to improve ultra-tightly coupled GPS-IMU and ESM performace. *ION NTM, San Diego, CA*, 24-26 January, (2005), 951 – 960.

Roark, R. J.; Young, W. C.: *Formulas for stress and strain*. McGraw-Hill, Auckland (1986).

Sasiadek, J. Z.; Wang, Q.: Fuzzy adaptive Kalman filtering for INS/GPS data fusion and accurate positioning. *Preprints of the 15th IFAC Symposium on Automatic Control in Aerospace*, Bologna: International Federation of Automatic Control, (2001), 410 – 415.

STM: *LIS1Y08AS4 Inertial Sensors*. Product Preview. Rev. 1.1. STMicroelectronics, Geneva (2004).

Wagner, J.: *Zur Verallgemeinerung integrierter Navigationssysteme auf räumlich verteilte Sensoren und flexible Fahrzeugstrukturen*. VDI-Verlag, Düsseldorf (2003).

Wagner, J.; Wieneke, T.: Satellite and inertial navigation - conventional and new fusion approaches. *Control Engineering Practice*, 11(5), (2003), 543 – 550.

Wagner, J. F.: Adapting the principle of integrated navigation systems to measuring the motion of rigid multi-body systems. *Multibody System Dynamics*, 11, (2004), 87 – 110.

Yi, Y.; Grejner-Brzezinska: Performance comparison of the nonlinear Bayesian filters supporting GPS/INS integration. *Proceedings of the ION NTM 2006*, The Institute of Navigation, Fairfax/VA, (2006), 977 – 983.

Address: Dipl.-Ing. Thorsten Örtel and Prof. Dr.-Ing. Jörg F. Wagner, Institut für Statik und Dynamik der Luft- und Raumfahrtkonstruktionen, Universität Stuttgart, Pfaffenwaldring 27, D-70569 Stuttgart.
email: oertel@isd.uni-stuttgart.de; jfw@isd.uni-stuttgart.de